CHEMISTRY OF MATERIALS

Article

pubs.acs.org/cm

Densification of Ionic Liquid Molecules within a Hierarchical Nanoporous Carbon Structure Revealed by Small-Angle Scattering and Molecular Dynamics Simulation

José Leobardo Bañuelos,*[,†] Guang Feng,*[,‡] Pasquale F. Fulvio,[†] Song Li,[‡] Gernot Rother,[†] Sheng Dai,[†] Peter T. Cummings,[‡] and David J. Wesolowski[†]

[†]Chemical Sciences Division, Oak Ridge National Laboratory, Oak Ridge, Tennessee 37831, United States

[‡]Department of Chemical and Biomolecular Engineering, Vanderbilt University, Nashville, Tennessee 37235, United States

Supporting Information

ABSTRACT: The molecular-scale properties of the room temperature ionic liquid (RTIL) 1-butyl-3-methylimidazolium bis(trifluoromethylsulfonyl) imide, $[C_4mim^+][Tf_2N^-]$, confined in nanometer-scale carbon pores have been investigated using small-angle X-ray and neutron scattering and fully atomistic molecular dynamics simulations. $[C_4mim^+][Tf_2N^-]$ densities significantly higher than that of the bulk fluid at the same temperature and pressure result from the strong affinity of the RTIL cation with the carbon surface during the initial filling of slitlike, subnanometer micropores along the mesopore surfaces. Subsequent filling of cylindrical ~8 nm mesopores in the mesoporous carbon matrix is accompanied by weak RTIL densification. The relative size of the micropores compared to the ion dimension, and the strong interaction between the RTIL and the slit-like micropore, disrupt the bulk RTIL structure. This results in a low-excluded volume, high-RTIL ion density configuration. The observed interfacial phenomena are simulated using a molecular dynamics model consisting of a linear combination of mesopore and micropore effects. These observations highlight the importance of including the effects of a porous substrate's internal surface morphology, especially roughness and microporosity, on the resulting electrolyte structural properties and performance in electrical energy storage applications.

KEYWORDS: *room temperature ionic liquid, mesoporous carbon, energy storage, interfacial structure, nanoconfinement*

INTRODUCTION

One major challenge in meeting the demands of a technology-driven global society is the ability to efficiently store energy and make it available in low-cost, compact, high-power-density platforms, for use in industrial and consumer applications in devices ranging from portable electronics to electric vehicles. Supercapacitors, also called electrical double-layer capacitors (EDLCs), have attracted great interest for their high power handling and long cycle life compared to batteries.[1,2] However, substantial improvements in their energy density, which largely depend on the component materials' voltage stability and electrolyte-accessible surface area,[3−5] are required to accelerate their implementation.

The rational design of next-generation energy storage devices, such as supercapacitors, requires a molecular-level understanding of the structure and dynamics of the electrolyte in the bulk phase and at the electrode interface where energy is stored. Room-temperature ionic liquids (RTILs), which are molten salts that remain in the liquid phase near room temperature, have emerged as promising electrolytes due to their extremely low vapor pressure, excellent thermal stability, and high electrochemical stability at electrode potentials of up to 4 V without decomposition.[6−9] The ideal electrodes for these systems have high electrical conductivity and surface area, and easily accessible paths for electrolytes to reach these surfaces.[10−13] However, the highly porous networks of many electrode materials impose transport and nanoconfinement effects on the electrolytes which may alter the predicted performance. Commonly used classical electrochemical theories describe ions in the dilute solution limit at continuous, unstructured surfaces.[14,15] Yet it is unclear whether these classical descriptions apply to RTIL electrolytes at the complex surfaces of real electrode materials. The development of mesoporous carbons with good electrode properties and highly tunable morphologies,[16−18] combined with small-angle scattering and simulation studies, provides new insights into RTIL structural properties at complex, nanotextured interfaces.

The molecular structure of many RTILs results from the interplay of electrostatic and van der Waals forces of the polar sites and the alkyl chains, respectively.[19−22] Several computational studies have probed the structural and dynamic properties of RTILs in contact with graphene/graphite surfaces,[23−25] nanotubes,[26−29] slit pores,[30,31] mesoporous carbon,[32] and realistically modeled electrodes.[33] These studies found that RTILs are strongly attracted to graphite, forming a dense sorption layer with ca. one nm thickness.[24,25,34,35] The graphite surface also induces strong interfacial layering of RTILs. An approximately three-molecular-layer-thick[36] interfacial layer is formed that has significantly slower dynamic properties compared to the bulk. Atomic force microscopy (AFM) and surface force apparatus (SFA) measurements, combined with molecular dynamics (MD) simulation, have

Received: October 24, 2013
Revised: December 18, 2013
Published: December 19, 2013

been reviewed recently by Perkin.[37] The AFM studies emphasize that the ion layering structure depends on surface chemistry, temperature, surface charge and ion type, and that this layering structure is at least an order of magnitude larger than the single ion layer thickness. Dynamic SFA experiments show increased viscosity, yet good lubrication at the interface.[37] Materials used as supercapacitor electrodes are composed of high surface area carbon particles having internal pores and the effects of confinement on the density, viscosity, and diffusion of the electrolyte confined in nanopores are of great importance for the development of energy storage devices.

This communication reports on the structural properties of the RTIL $[C_4mim^+][Tf_2N^-]$ confined in soft-templated mesoporous carbon.[16,17] For $[C_4mim^+][Tf_2N^-]$, thermophysical properties have been studied,[38−40] the structure by X-ray scattering has been obtained,[41,42] and optimized potentials have been developed[43−47] to describe this liquid in the bulk state. Because the bulk fluid properties are well-understood, its choice in the current work forms a solid basis for exploring RTIL properties at textured interfaces and under nanoscale confinement. The template-synthesized porous carbon used in this study consists of uniform cylindrical mesopores as well as small micropores and has favorable electrical and structural properties which allow fast ion and electron transport. Mesopores are defined as pores with sizes between 2 and 50 nm, whereas micropores are pores with sizes smaller than 2 nm.[48] Along with other new carbon materials, this class of materials has attracted interest as electrode materials for electrochemical capacitors.[16]

To separate the geometric confinement effects from those of the carbon surface on the RTIL structure, we performed measurements on samples filled with various amounts of RTIL inside the porous carbon matrix. Small-angle scattering provides structural information about the ionic liquid and host mesoporous matrix from the subnanometer to several hundred nanometer length scales, and is used here to measure how RTIL density changes within the porous network. The MD simulations presented herein incorporate validated force fields[49,50] into analogous physical models and are used to verify the structural information from small angle scattering. The observations contained in this study shed light on understanding the properties of the RTIL−solid interface and bear relevance to diverse applications involving the use of RTILs in heterogeneous media such as nanoparticle synthesis, hydrolysis, and flexible supercapacitor fabrication.[51−55]

EXPERIMENTAL SECTION

Materials Synthesis and Preparation. The mesoporous carbon (MC) was synthesized using a soft-templating synthesis method.[17,18] The MC was prepared by the self-assembly of resorcinol (Sigma-Aldrich, 99%) and formaldehyde (Sigma-Aldrich, 37 wt %) in the presence of triblock copolymer Pluronic F127 (EO_{106}-PO_{70}-EO_{106}, BASF) purchased from Sigma-Aldrich according to previously reported recipes.[18,56] In a typical synthesis, approximately 1.1 g of resorcinol and 1.1 g of Pluronic F127 were dissolved in 4.5 mL of ethanol, 3.4 mL of water, and 1.1 mL of concentrated HCl (37 wt %). To this, 1.3 mL of formaldehyde solution (37 wt %) was added and the system was stirred until phase separation was observed. After stirring for an additional 12 min, the suspensions were centrifuged at 9500 rpm for 5 min and the aqueous phases were discarded. The isolated polymer-rich phases were quickly redispersed using minimal amounts of ethanol with stirring followed by casting on Petri dishes. Thin films were cured at room temperature overnight and at 80 °C for 24 h. The phenolic resin-triblock copolymer nanocomposites were finally carbonized at 400 °C for 2 h (1 °C/min heating rate) and 850 °C for 2 h in flowing nitrogen and using 2 °C/min as heating rate. The MC was labeled MC-127 for the F127 triblock copolymer used to prepare it. $C_4mim.Tf_2N$-D_{15} was prepared from $C_4mim.Br$-D_{15} (Isotec Stable Isotopes) via a modified anion exchange procedure[57] using lithium bis(trifluoromethylsulfonyl) imide (3M) in D_2O instead of H_2O.

To prepare the ionic liquid-MC composites, a 1.5 mol/L solution of deuterated C4mim.Tf2N-D15 in deuterated methanol-D_4 (Alfa Aesar, 99.8% isotopic) was prepared. The amount of solution added to each MC sample was calculated assuming a bulk density of 1.4904 g/cm^3 for the ionic liquid, and to completely fill the micropores of the MC material in addition to the different percentages of the mesopore volumes. Sample mixing was performed using a combination of magnetic stir bar in a sample vessel, followed by sonication at 60 °C for 30 min. This mixing cycle was repeated three times before placing the sample in a vacuum oven at 1 mbar and 70 °C for 48 h. The oven temperature was lowered to 23 °C and samples were allowed to equilibrate for several hours before filling the oven with argon gas to achieve ambient pressure and an inert atmosphere for sample transfer into the glovebag. In all small-angle scattering measurements, care was taken to avoid introducing water adsorption from the atmosphere in the bulk liquid and powder samples. Prior to loading into measurement cells, the empty powder was dried under vacuum for at least 24 h at 100 °C. All samples were loaded into measurement cells under an argon atmosphere.

Gas Physisorption Characterization. Nitrogen adsorption isotherms were measured for the empty porous matrix as well as the RTIL-imbibed samples. Nitrogen adsorption isotherms were measured at −196 °C using an Autosorb-1 gas sorption system manufactured by the Quantachrome Corp. (Boynton Beach, FL). Before adsorption measurements, the powders were degassed under vacuum (~1×10^{-5} Pa) for 12−24 h at 110 °C.

CHN Elemental Analysis. Carbon, hydrogen, nitrogen (CHN) analysis by combustion was also carried out to obtain an accurate estimate of the ionic liquid to mesoporous carbon ratios for each MC-127 powder imbibed with different RTIL amounts. The CHN analysis measurements were performed by Elemental Analysis, Inc. (Lexington, KY) using a 2400 Perkin-Elmer CHN Analyzer. The total mass fractions of C, H, and N were obtained for each RTIL/MC-127 composite, as well as for the bulk RTIL. The carbon and nitrogen ratios between the RTIL/MC-127 composites, the empty MC-127, and the bulk RTIL were compared to obtain estimates of the mass fraction of RTIL within each sample.

Small-Angle Scattering. Small-angle scattering intensity as a function of momentum transfer, Q was collected for each sample (Q is related to the d-spacing, scattering angle (2θ), and radiation wavelength (λ), via $Q = 2\pi/d = 4\pi\sin(\theta)/\lambda$). Small-angle X-ray scattering (SAXS) measurements on the dry MC-127 sample and samples with different pore loadings, S_1, S_2, S_3, and S_4 of $[C_4mim^+][Tf2N^-]$ were carried out using the Anton Paar SAXSess mc^2 instrument at the Center for Nanophase Materials Sciences at Oak Ridge National Laboratory. The instrument uses a tube source equipped with multilayer optics and tuned to the Cu kα wavelength. Measurements were conducted at 20 kV and 50 mA. An image plate was used to record the data. The powder samples were sealed in a custom-made sample holder consisting of polyimide tubing, sealed at both ends using HPLC tubing stainless steel fittings. Raw scattering data corrections included normalization to the incident beam intensity and sample attenuation by collecting counts behind the transparent nickel beam stop, empty container background scattering subtraction, dark current subtraction, and detector efficiency corrections. Water scattering was used to calibrate all scattering intensities to absolute units of differential scattering cross section per unit volume, $I(Q) = (1/V)d\Sigma/d\Omega$ (cm^{-1}).

Small-angle neutron scattering (SANS) measurements were conducted at BL-6B (EQ-SANS), Spallation Neutron Source, ORNL. Measurements were conducted in two configurations: (1) 1.3 m sample to detector distance (SDD), with wavelength band of 1.13−4.65 Å; and (2) 4 m SDD, using frame-skipping mode, which

dx.doi.org/10.1021/cm4035159 | Chem. Mater. 2014, 26, 1144−1153

simultaneously uses two wavelength bands, 2.61−5.61 Å and 9.51−12.91 Å, to obtain a wide Q-range and sufficient overlap in Q between configurations. Samples were loaded into 1 mm path length, 18 mm diameter, quartz banjo cells. The beam size at the sample position was defined by an aperture of 10 mm in diameter. Standard corrections for background, detector efficiency, and intensity calibrations were performed. A Vycor glass standard was used to place the data on an absolute scale. For both SAXS and SANS measurements, the total mass of each sample was recorded to obtain a value for the packing density, and by combining with elemental analysis data for each sample, the mesoporous carbon mass was extracted and used to normalize the scattering data.

Invariant Calculation. The invariant was determined from $Q = 0$ to ∞ by extrapolating the unmeasured low-Q and high-Q regions of the scattering using Guinier and Porod extrapolations,[58] respectively. First, the low-Q particle scattering and high-Q molecular scattering contributions were subtracted. The Porod contribution due to the powder grain scattering at low-Q (0.007−0.013 Å^{-1}) was fit using a Porod law, AQ^{-p}, and subtracted from the scattering data, leaving only the forward scattering contribution of the mesophase. The forward scattering was extrapolated to $Q = 0$ using the Guinier fit[58] to data from $Q = 0.007$ to 0.013 Å^{-1}. At high Q (0.4−0.55 Å^{-1}), the scattering was fit using $AQ^{-p} + B$, where B is the approximately constant scattering due to incoherent scattering and to the forward scattering of the atomic scale structure factors in the composite. The factor B was subtracted and the high-Q region was extrapolated using the Porod law,[58] with an exponent of 4 from $Q = 0.55$ Å^{-1} to ∞. The same Q ranges were chosen for all sample calculations.

Modeling Setup. The mesopore was modeled by three-layer carbon nanotubes (CNTs) with a 0.341 nm gap between neighboring walls. To obtain the right number of ion pairs inside mesopore, we connected the simulation to a RTIL reservoir which allowed the ions freely enter or leave the mesopore. Then, the reservoir was removed to leave the system containing the mesopore and RTILs inside. The different mesopore loading fractions (f_{meso} = 0.16, 0.42, 1.0) were determined by removing the number of ions with respect to the total number of ions in the full loading case. The micropore was modeled by a slit of two walls separated by a 0.75 nm distance and each wall was modeled by three-layer graphene sheet. To guarantee that ions can automatically fill the pore, the slit-shaped micropore was connected with a reservoir as well. MD simulations were performed in the canonical ensemble using a user-modified version of MD package GROMACS.[59] Periodic boundary conditions were used in three dimensions. The force fields for the electrode atoms (carbon) and ions in $[C_4mim^+][Tf_2N^-]$ were the modified Atomistic Polarizable Potential for Liquids, Electrolytes and Polymers (APPLE&P) developed by Borodin.[60,61]

The electrolyte temperature was maintained at 300 K using the Berendsen thermostat. The electrostatic interactions were computed using the PME method.[62] Specifically, an FFT grid spacing of 0.1 nm and cubic interpolation for charge distribution were used to compute the electrostatic interactions in reciprocal space. A cutoff distance of 1.1 nm was used in the calculation of electrostatic interactions in the real space. The nonelectrostatic interactions were computed by direct summation with a cutoff length of 1.1 nm. The LINCS algorithm[63] was used to maintain bond lengths in the C_4mim^+ and Tf_2N^- ions. To achieve equilibration, the mesopore and micropore systems were each first run for 6 and 12 ns, respectively, and then a 9 ns production run was performed. Herein, the equilibrium state was determined by the fact that the ion density obtained during different time intervals (e.g., 0−3 nm, 3−6 nm, and 6−9 nm) after equilibrium changed very little.

The mean density ρ'_{MD} (Figure 3) was calculated directly from the number density (Figure 6) for the micropore and mesopores with f_{meso} = 1.0 and 0.42. The first layer RTIL coverage in the mesopore with f_{meso} = 0.16 is incomplete and a correction to account for a void on the mesopore surface was carried out to obtain the number density. It is difficult to assess the magnitude of the void space because it depends on detailed knowledge of the orientation and relative arrangement of ions within the adsorbed layer and on the variation of the shape and location of the void space over time. A series of simulations between f_{meso} = 0.16−0.42 show complete coverage at $f_{meso} \approx 0.3$. Thus, the density in the f_{meso} = 0.16 simulation is scaled by 0.3/0.16, or 1.875, to exclude the void in the first layer.

RESULTS AND DISCUSSION

Empty Mesoporous Carbon Structure. First, the pore structure of MC-127[16,17] was characterized using both N_2 gas adsorption and SAXS. The MC-127, which is obtained from the carbonization of a polymer-templated phenolic resin, consists of an array of uniform-size cylindrical mesopores, as well as micropores distributed throughout the porous network.[16] The pore sizes, specific volume and surface area, and ratio of micropores to mesopores are tunable depending on the synthesis conditions. N_2 adsorption isotherm analysis provided micropore and mesopore specific volumes and surface areas, as well as the pore size. The micropore volume, v_{mi} = 0.045 cm^3/g, micropore surface area, S_{mi} = 330 m^2/g, and external surface area, S_{ex} = 9 m^2/g, were all obtained using the αs-plot method[64] using a nonporous carbon as a reference (v_{mi} and S_{mi} were calculated in the αs-plot range of 0.75−1.00, and S_{ex} in the range of 2.5−7.5). The total pore volume, v_{TOT} = 0.53 cm^3/g, was obtained from the total adsorbed volume at relative pressure p/p_0 = 0.97 (single-point pore volume). The mesopore width, w_{KJS} = 7.8 nm, was calculated using the Barrett−Joyner−Halenda (BJH) algorithm for cylindrical pores according to the improved Kruk-Jaroniec-Sayari (KJS) method.[65,66] The specific surface area, S_{BET} = 440 m^2/g, was obtained by the Brunauer−Emmett−Teller (BET) method in the relative pressure range of 0.05−0.20.[67] The v_{mi}/v_{TOT} ratio is 0.085, with the remaining volume comprised by cylindrical mesopores with an average diameter of 7.8 nm. The S_{ex}/S_{BET} ratio shows that the external surface of the powder grain is a minor contribution to the total surface area and that 98% of the surface area in this material is in the internal pore structure.

Small-Angle Scattering. Small-angle scattering is useful in that (1) it is not restricted to the study of simple model geometries, (2) in many cases provides the necessary contrast to study fluids under confinement, and (3) has high penetration strength and is not limited by surface attenuation effects. As a bulk structural probe, it also provides representative microstructural information over the entire sample instead of sampling a small spatial region. SAXS and SANS are complementary techniques for the characterization of complex nanoporous materials.[68−70] In SAXS, the interaction is with the electron density, thus dependent on the atomic number of the components of the system. On the other hand, in SANS the interaction is with the nucleus, and thus sensitive to isotopic substitution as well as light elements such as hydrogen. In the empty porous carbon, the strength of the signal originates from the contrast between the nanostructured carbon material and the empty space in the pores. The change in scattering contrast as RTIL is introduced into the porous system result in intensity variations that are similar in magnitude for both SAXS and SANS measurements; thus, SAXS results are primarily presented with SANS providing additional independent support of observations.

The empty mesoporous carbon SAXS data, labeled MC-127 (after the F127 polymer template), is shown in Figure 1. Several distinguishing features allow characterizing its porosity, pore morphology, and pore surface characteristics. The peak at $Q = 0.058$ Å^{-1} corresponds to correlations between the uniform size cylindrical mesopores.[17,18] The scattering intensity $I(Q)$ follows a power law decay, $I(Q) \approx Q^{-p}$, at low-Q from 0.007 to

dx.doi.org/10.1021/cm4035159 | Chem. Mater. 2014, 26, 1144−1153

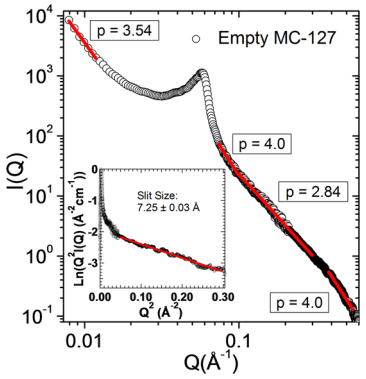

Figure 1. SAXS curve of empty MC-127 nanoporous carbon. The scattering exponents indicate rough (p = 3.54) and smooth (p = 4.0) surfaces, and mass fractal (p = 2.84) scattering at different length scales. The primary peak at Q = 0.058 Å^{-1} corresponds to pore−pore correlations within the mesophase, while the scattering from 0.2 to 0.6 Å^{-1} is due to micropores decorating the mesopore surface. Inset: ln(Q^2 * $I(Q)$) vs.Q^2 plot, showing a modified Guinier analysis (solid line) fit, indicating 7.25 Å slit-like micropores.

0.013 Å^{-1}. The exponent value p = 3.54 in this region corresponds to a rough external surface for the mesoporous micrometer-scale powder particle (values from 3 to 4 correspond to rough and smooth surfaces, respectively). The scattering at Q values from 0.07−0.6 Å^{-1} contains information about the surface morphology of the mesopore walls, including the presence of micropores in the system. The intensity of these features is proportional to the square of the scattering length density (SLD) difference, $\Delta\rho^*$, between the carbon and the void space, i.e., the empty pores.

Pore Structure. The pore structure of the mesoporous carbon is characterized by (1) the pore volume fraction, obtained from the scattering invariant from the normalized intensity curve, $I(Q)$, and applying the two-phase invariant formula, (2) analyzing the power law dependence of the scattering to characterize the pore wall morphology, (3) and applying a modified Guinier analysis[71,72] to estimate the geometry of micropores in this system.

The scattering invariant, Z, relates the scattered intensity, $I(Q)$, to the volume fraction, φ_1, of a two phase system through the following relation: $Z = \int_0^\infty Q^2 I(Q)dq = 2\pi^2\varphi_1(1-\varphi_1)(\rho_1^* - \rho_2^*)^2$. This relation was used to calculate the volume fraction of the carbon phase φ_1, and the empty space $1-\varphi_1$, from the scattering of the empty MC-127. Here, $(\rho_1^* - \rho_2^*)$ is the difference in the SLD between the two components. The neutron SLD of phase j, ρ_j^*, was obtained from $\rho_j^* = \Sigma_{i=1}^{N} b_i(\rho_j N_A)/(M_j)$, where b_i is the coherent scattering length of the ith atom, N is the total number of atoms in the molecule which comprises phase j, ρ_j is the mass density, and M_j is the molar mass. For carbon, N = 1, and for the RTIL phase discussed later, N corresponds to all the atoms in the cation and anion combined. To calculate the X-ray SLD, the b values in the expression were replaced by Zr_e, where Z is the atomic number of the ith atom and r_e is the classical radius of the electron. The total pore volume obtained from this calculation is 0.53 cm^3/g; in agreement with the N_2 adsorption results discussed previously. A narrow region from 0.073 to 0.1 Å^{-1} in the dry MC-127 pattern exhibits a Q^{-4} power law decrease in the scattering intensity, following Porod's law:[73,74] $I(Q) = 2\pi\Delta\rho^2 S_{ij} Q^{-4}$ (S_{ij} is the surface area between phases i and j). The surface area calculated in this region in Figure 1 using Porod's law is 65 m^2/g.

From 0.1 to 0.3 Å^{-1}, the scattering decays with a power law of 2.84 (Figure 1), corresponding to scattering characteristic of a mass fractal (values of less than 3 correspond to mass fractals).[75−77] The interaction between the phenolic resin and triblock copolymer template during annealing, and the rearrangement of carbon atoms during carbonization imprint a complex morphology at the pore surface. This gives rise to the compact mass fractal scattering in this region. A second Porod region with a scattering exponent of 4 is found in the micropore range for Q values 0.38−0.55 Å^{-1}. Fitting of the Porod law in this region yields a surface area of 320 m^2/g, in close agreement with the micropore surface area of 330 m^2/g, obtained from N_2 gas adsorption. The best fit of a modified Guinier analysis,[71,72] conducted in the 0.22−0.54 Å^{-1} range, yields a 7.25 Å slitlike pore as a characteristic size scale and morphology for the microporosity (Figure 1, inset). The range of this fit covers the dominant features of the scattering from the micropore form factor, including the Porod scattering from the micropore surface; this range also shows a scattering intensity decrease with RTIL loading (discussed later), indicative of micropore filling. Fits to spherical and cylindrical objects yielded poor fits and the result for sheetlike forms yielded the most applicable model with a $Q_{max}R_t$ value of 1.14. This is within the required

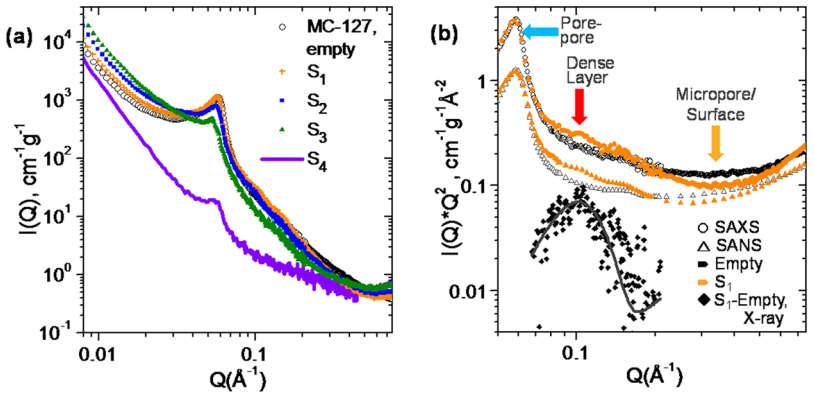

Figure 2. (a) SAXS plots of empty MC-127 and RTIL-imbibed mesoporous carbon samples (S1, S2, S3, S4). (b) $I(Q)Q^2$ vs Q, SAXS (○) and SANS(△), plots comparing dry mesoporous carbon (black) with the low loading, S1, sample (orange). The SAXS difference curve (◆) highlights the location (black line is a Gaussian fit centered at Q = 0.102 Å^{-1}) of the dense RTIL layer. At Q > 0.6 Å^{-1}, the scattering is the result of dry carbon and ionic liquid molecular-scale structure.

dx.doi.org/10.1021/cm4035159 | Chem. Mater. 2014, 26, 1144−1153

limit of $Q_{max}R_t < 1.3$ in order for the analysis to be applicable. The significant amount of microporosity (8.5%) in the carbon host is a factor to consider in the analysis of the organization of ionic liquids near the surface as will be discussed.

RTIL Structure in Pores. The effect of filling the carbon nanopores with RTIL on the regions of the scattering profile corresponding to cylindrical mesopore-mesopore correlations, mesopore surface scattering, and micropores decorating the mesopore surfaces, is discussed below. Details of the MC-127/$[C_4mim^+][Tf_2N^-]$ sample preparation are given in the Experimental Section. The samples were prepared by mixing empty MC-127 with deuterated methanol solutions containing measured amounts of fully deuterated (98% isotope purity) $[C_4mim^+][Tf_2N^-]$ corresponding to varying levels of total pore volume filling. Following mixing, the samples were placed under vacuum at 1 mbar and at 70 °C for at least 48 h to remove the solvent. All sample preparation and handling was performed under an inert atmosphere to avoid moisture contamination. SAXS data for the RTIL-imbibed samples, as well as the empty substrate, are plotted in Figure 2a. The samples are labeled S_1, S_2, S_3, and S_4, and each correspond to a RTIL volume filling fraction, f_{RTIL}, of 0.08, 0.2, 0.5, and 0.96, respectively (details of f_{RTIL} are shown in the following section).

The $I(Q)$ of the RTIL-loaded samples exhibits changes in several Q regions. At low Q, between 0.008 and 0.014 Å^{-1}, the variations in $I(Q)$ reflect the changes in the overall composition of the porous particle as it is filled with RTIL. The decrease in $I(Q)$ at values near the primary peak at 0.058 Å^{-1} is due to mesopore filling. Pore surface wetting, micropore saturation, and the presence of densification of RTIL ions at the surface leave signature contributions in $I(Q)$ in the Q range of 0.07−0.6 Å^{-1}. The variation in $I(Q)$ and in the mean pore density (discussed later) as f_{RTIL} is varied clearly shows that RTIL is covering the pore surfaces uniformly rather than completely filling some pores and leaving other pore surfaces unsaturated.

Evidence of attractive interactions between the RTIL and carbon surface is found by comparison of the empty and S_1 sample small-angle scattering data, shown in Figure 2b. The SAXS and SANS scattering data, displayed in the Kratky ($I(Q)$ Q^2 vs Q) representation, highlight the high-Q region of the measured profile. Both data sets show little intensity change in the mesopore center−center correlations at Q = 0.058 Å^{-1} upon loading with 0.18 g/g (RTIL/MC-127). This shows that the average SLD in the mesopore has not changed much. However, the region from 0.2−0.6 Å^{-1} shows diminished intensity, indicative of pore surface wetting and micropore saturation with RTIL. Once this surface is saturated, the intensity in this Q range does not change as RTIL filling increases; only small intensity increases occur for Q > 0.4 Å^{-1} due to the structure of the RTIL itself. An additional broad correlation emerges noted by an increase in intensity over the range 0.07−0.18 Å^{-1} with a maximum at approximately 0.1 Å^{-1}. The periodicity of this extra correlation, obtained by fitting a Gaussian function to the difference curve of the dry and RTIL-loaded samples, is approximately 6 nm. The presence of a similar additional correlation has been observed in studies of phase separation in binary mixtures under nanoconfinement[78] and attributed to the formation of a sorption phase at the pore surface. In both cases, the additional correlation arises because of the presence of a near-surface phase within the ordered porous medium. The SLD of the near-surface phase is very different from the SLD of the phase near the center of the pore, and this gives rise to the additional correlation, albeit by different mechanisms in each case.

The RTIL ions in the micropores create a region of high SLD contrast with the void space at the center of the mesopore. This increases the visibility of the MC-127's higher-order reflections. The higher order reflections are observed as slight modulations on the broad correlation noted previously, at approximately 0.11 and 0.153 Å^{-1}. The positions of these weak reflections agree with overlapping (110) and (200) reflections at 0.11 Å^{-1} and with the (210) reflection at 0.153 Å^{-1} of a *p6/mm* symmetry mesophase (Figure 2b). Hence, the contrast between the RTIL-filled micropores along the carbon surface and the empty space at the center of the pore permits a more clear identification of the long-range ordering of the mesopores in the substrate. Given the periodicity of the pore−pore correlation at Q = 0.058 Å^{-1}, the periodicity of the broad correlation at Q = 0.1 Å^{-1}, and the observed variation in scattered intensity between MC-127 and S_1, the broad correlation in the S_1 sample is described as a dense phase with a maximum density along the inner surface of the mesopore wall.

RTIL Mean Pore Density. Calculating the invariant directly from scattering data provides a route to estimate the volume fraction of different phases in a material and is used here to calculate the mean density of RTIL in the porous system. An advantage of using the invariant is that it does not assume specific shapes to the components involved. Also, because the mass fractions are well-known from the sample preparation and composition analysis, the RTIL density under confinement may be calculated without further assumptions. The invariant of a three phase system has been derived by Wu[79] and considers the relative volume fractions φ_i and SLDs ρ_i^* of each phase: $Z = 2\pi^2[\varphi_1\varphi_2(\rho_1^* - \rho_2^*)^2 + \varphi_2\varphi_3(\rho_2^* - \rho_3^*)^2 + \varphi_1\varphi_3(\rho_1^* - \rho_3^*)^2]$. It is used here to treat the MC-127/RTIL system, where the subscripts 1, 2, and 3 correspond to the carbon, void, and RTIL phases, respectively. The normalized volume in terms of the volume fractions is expressed as $\varphi_1 + \varphi_2 + \varphi_3 = 1$ and the RTIL mass density in terms of the SLD is given by $\rho_3 = ((\rho_3^*)/(\rho_{IL}^*))$ (ρ_{IL}^* is the bulk RTIL SLD value). The three expressions above, combined with the relation between the invariant and scattering intensity introduced earlier, were used to calculate the volume fraction, φ_3, of the RTIL phase under confinement.

The density of the RTIL phase confined in the porous network is discussed below. The mean RTIL density with respect to the bulk density is defined as ρ_{pore}/ρ_{bulk}. The RTIL filling fraction is defined as $f_{RTIL} = \varphi_3/(1 - \varphi_1)$, i.e., the normalized volume fraction of RTIL divided by the normalized total pore space. φ_3 and ρ_{pore} are obtained directly from the scattering analysis. The normalized total pore space, $1 - \varphi_1$, corresponds to v_{TOT} = 0.53 cm^3/g from the characterization of the empty MC-127 discussed earlier. Figure 3 shows ρ_{pore}/ρ_{bulk} vs f_{RTIL} obtained from the analysis of the experimental data; it is labeled ρ'_{SAXS} to distinguish it from the simulation data (discussed later). The f_{RTIL} values obtained for samples S_1, S_2, S_3, and S_4 are 0.08, 0.2, 0.5, and 0.96, respectively. The large increase at f_{RTIL} = 0.08, is primarily due to the local intermolecular packing of ions in the micropores, as supported by observations from scattering of the S_1 sample (discussed in the previous section). The nitrogen adsorption analysis (discussed later) shows that 91% of the pore space is accessible to N_2 adsorption in the S_1 sample. The adsorption isotherms also show that most of the micropore volume is inaccessible in the S_1 sample due to RTIL filling. The densification is partly

dx.doi.org/10.1021/cm4035159 | *Chem. Mater.* 2014, 26, 1144−1153

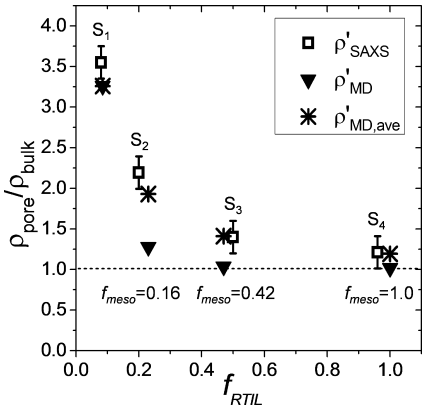

Figure 3. Plot of ρ_{pore}/ρ_{bulk} vs f_{RTIL}. Experimentally measured RTIL mean density ρ'_{SAXS} (□). CMD-obtained mean density ρ'_{MD}(▼) for the micropore and each mesopore loading. The average mean density, $\rho'_{MD,ave}$ (*) obtained as linear combination of the CMD-modeled micropore and mesopore RTIL densities. For the micropore, $\rho'_{MD,ave} = \rho'_{MD}$.

due to the micropores' ability to disrupt the bulk ion coordination structure as will be later discussed. This is an interfacial phenomenon and cannot be taken as a statement on the compressibility of an RTIL in the bulk state.

Particle Composition Changes. The increase in intensity at low-Q values (0.008−0.014 $Å^{-1}$ in Figure 2 and Figure 4) as

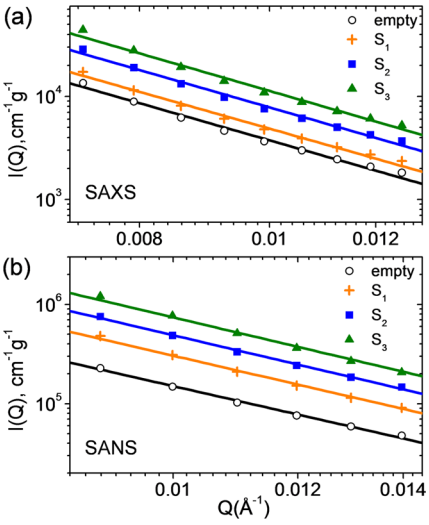

Figure 4. (a) SAXS and (b) SANS low-Q part of scattering data. The variations in intensity as a function of pore loading result from the scattering contrast difference between average scattering length density of the RTIL-filled carbon particle and air. Symbols are experimental data and lines are fits using a Porod model that uses the contrast between the RTIL/MC-127 composite particle and air Δp^*_{p-a}, for both (a) X-rays and (b) neutrons. The variations in low-Q intensity agree with the expected change in contrast due to the change in composition as a function of RTIL filling.

a function of RTIL filling is due to the changing composition of the nanoporous carbon particle and its resulting scattering contrast with the air interface. The carbon, empty space, and RTIL volume fractions, φ_j, and densities, ρ_j, obtained in the previous section were used to calculate an average particle SLD: $\rho^*_p = \varphi_{carbon}\rho^*_{carbon} + \varphi_{air}\rho^*_{air} + \varphi_{RTIL}\rho^*_{RTIL}$, where ρ^*_j is the X-ray or neutron scattering length density of each component. The SLD for air is defined to be zero in this case because of its low interaction cross-section. A Porod model, $I(Q) = A(\Delta\rho^*_{p-a})^2 Q^{-p}$, in which A is a constant, $\Delta\rho^*_{p-a} = \rho^*_p - \rho_{air}$, and p is the scattering exponent, reproduces both the SAXS and SANS experimental data, as shown in Figure 4. The scattering between the RTIL/MC-127 composite and air interface causes increased scattering with RTIL filling. Overfilled samples, on the other hand, introduce excess RTIL outside the particle surface, decreasing the composite's contrast and the scattering intensity at low-Q values; Figure S1 in the Supporting Information shows the effect of overfilling to 140% and 210% of the amount used in sample S_4. The low-Q intensity continues to decrease as excess RTIL replaces the empty space in macropores between the powder particles. However, if RTIL is added beyond the limit when the pore system becomes full, the intensity at the primary peak no longer decreases and remains constant since RTIL is no longer entering the pores. S_4 and the two overfilled samples showed approximately the same intensity at the primary peak position. The increase in intensity at the lowest Q values can thus be attributed to changes in particle's composition as the porous network fills with RTIL.

Nitrogen Adsorption of RTIL/MC_{-127} Composites. Nitrogen adsorption isotherms were obtained for samples S_1−S_3 and compared with MC-127, and are shown in Figure 5a.

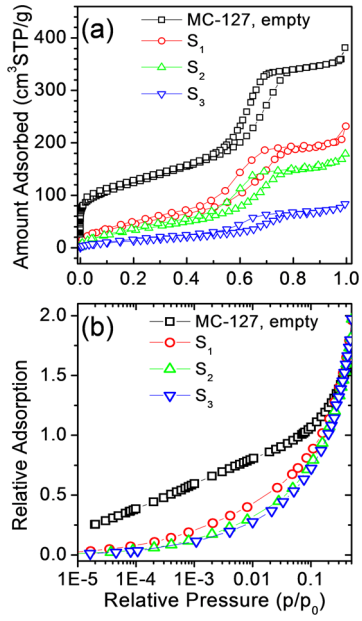

Figure 5. (a) N_2 adsorption isotherms for the empty MC-127 nanoporous carbon and samples S_1, S_2, and S_3 showing the decrease in N_2 uptake and hysteresis behavior. (b) Relative adsorption isotherm (normalized by the monolayer capacity obtained from the BET equation) in the low pressure range, shows modification of the pore surface upon RTIL loading. Both a and b are normalized by the total sample mass.

Because nitrogen is not miscible with this class of ionic liquids,[80] the N_2 accessible volumes obtained from adsorption data analysis of the RTIL-filled samples provide a useful comparison[81] with the void space volumes obtained from the scattering data. The RTIL/MC-127 composite mass-normalized isotherms are all type IV with H1 hysteresis loops characteristic of samples with large mesopores.[67] In the latter, the capillary condensation steps do not shift much with respect to each other, although broadening of the condensation steps

dx.doi.org/10.1021/cm4035159 | Chem. Mater. 2014, 26, 1144−1153

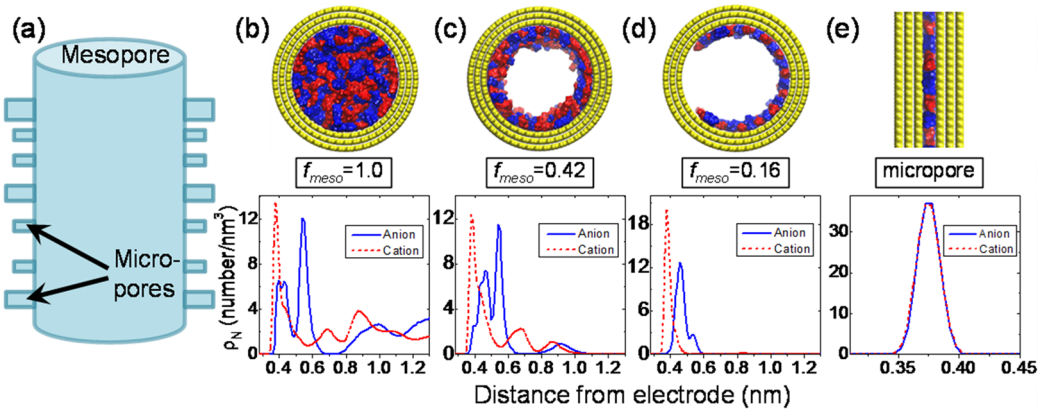

Figure 6. (a) Structural model showing the mesopore and micropore components in the MC-127 system. (b–d) Simulation snapshots (top) and ion density distributions (bottom) for $[C_4mim^+][Tf_2N^-]$ inside mesopores with pore loadings 1.0, 0.42, and 0.16, respectively. (e) Simulation snapshot (top) and ion density distribution (bottom) inside the 0.75 nm carbon micropore. The yellow spheres represent the pore confinement; the red and blue components denote C_4mim^+ and Tf_2N^- ions, respectively.

considerably increases with respect to the empty MC-127. The N_2 adsorbed volume for S_1, after normalizing to the carbon mass, is 91% of the value measured for MC-127. This is close to the 92% empty pore space obtained from the scattering analysis. No N_2-accessible pore volume was measurable for the sample with the highest filling, S_4, consistent with complete pore-filling. The N_2 accessible volumes for S_2 and S_3 were reduced with RTIL filling. The values for S_2 and S_3 were 0.336 and 0.146 cm^3/g_{carbon}, compared to the void space values of 0.425 and 0.266 cm^3/g_{carbon}, obtained from the scattering analysis. At low RTIL loading (in S_1), N_2 is able to access much of the mesopore volume, yet in S_2 and S_3 the increased RTIL volume likely blocks some of the mesopore openings which is manifested by the disagreement between the measured N_2 accessible volumes and the empty phase volumes obtained from the scattering analysis.

The vertical axis on the relative adsorption plot (Figure 5b) shows that N_2 forms a monolayer of gas (when relative adsorption = 1) on the empty MC-127 at slightly lower relative pressure than for the composites with IL. This means that the empty MC-127 has a higher adsorption capacity and consequently more hydrophilic surface[82,83] than the composites (N_2 is hydrophilic). For these composites, regardless of amount of ionic liquid added, the mesopore surfaces are clearly modified. Most of the RTIL adsorption to the carbon surface occurs in the S_1 sample because the largest change in relative adsorption occurs between the MC-127 and S_1 isotherms, followed by minor changes in the S_2 and S_3 isotherms in the low relative pressure region.

Several experimental observations were used to determine the organization of the RTIL within S_1 and are summarized below. From N_2 adsorption: (1) empty MC-127 v_{TOT} is composed of 8.5% micropores and 91.5% mesopores, (2) the N_2-accessible volume in the S_1 sample is 91% of v_{TOT}, and (3) the relative adsorption in the micropore region shows the greatest change between the MC-127 and S_1 data. The following were observed from scattering: (1) decreased intensity in the micropore region due to RTIL filling with the strongest changes between MC-127 and S_1, (2) the presence of an additional correlation due to dense RTIL layer formation in S_1, and (3) f_{RTIL} = 0.08 with $\rho_{pore}/\rho_{bulk} > 3$ for S_1. These experimental observations show that most of the RTIL in the S_1 sample is found within the micropore volume. Then, subsequent filling to higher f_{RTIL} proceeds primarily through the filling of mesopores in MC-127. The information from small-angle scattering, combined with adsorption data, provided constraints to build a sensible model using classical molecular dynamics simulation.

CMD Simulation. The experimentally obtained pore sizes for the carbon matrix were used as inputs to generate an analogous confining system consisting of mesopores and micropores (Figure 6) in the fully atomistic molecular dynamics (CMD) simulations. To simplify the simulation system, the micropore and mesopore were modeled separately. The micropore was considered to have full RTIL filling, while the mesopores each have a different RTIL pore volume fraction f_{meso}. The f_{meso} were chosen such that the normalized total RTIL filling fractions, $f_{RTIL} = v'_{mi} + f_{meso}v'_{meso}$, are close to the experimental f_{RTIL}.

Here, $v'_{mi} = v_{mi}/v_{TOT}$ = 0.085 is the normalized micropore volume obtained from gas adsorption analysis and $v'_{meso} = v_{meso}/v_{TOT} = 1 - v'_{mi}$ is the normalized mesopore volume. Mesopore f_{meso} values of 0.16, 0.42, and 1.0 were chosen in the simulation and correspond to f_{RTIL} values of 0.23, 0.47, and 1.0, respectively.

The mesopore was modeled by three-layer carbon nanotubes (CNTs) with a 0.341 nm gap between neighboring layers, with the diameter of the innermost tube matching the experimentally measured mesopore diameter. Micropores were modeled by a nanoslit pore consisting of two three-layer graphene walls separated by a 0.75 nm distance. The three-carbon-layer set up for both the mesopore and slit-shaped micropore models is used to more closely resemble the interaction between RTIL and a pore, instead of a nanotube or single graphene sheet.The simulation snapshots and resulting ion number density distributions (about the center of mass (COM)) for each f_{meso} are given in Figure 6b–d, as well as for the completely filled micropore (Figure 6e).

The distributions, ρ_N, show the alternating cation–anion structure in the mesopore (Figure 6b–d), with the cation closer to the wall than the anion in all three cases. The f_{meso} = 1.0 case shows a highly ordered structure near the pore wall, indicated by sharp peaks and large local densities. At further distances, the density as a function of distance from the electrode surface fluctuates near the bulk density. Though affected significantly as f_{meso} is reduced, the distributions are the net result of the RTIL

dx.doi.org/10.1021/cm4035159 | Chem. Mater. 2014, 26, 1144–1153

interacting with the pore wall and with itself. Confinement in subnanometer pores eliminates the alternating cation−anion structure normal to the pore wall[33] as shown in Figure 6e for RTIL in the 0.75 nm micropore. The resulting cation and anion distributions both show a higher-density maximum near the pore center.

Interestingly, the RTIL/micropore interaction potential, computed by the van der Waals interaction potential between ions and atoms of the carbon pore in the MD simulation, is 247 kJ/mol, which is higher than the standard molar enthalpy of vaporization which experiments and simulations estimate to be between 136 and 174 kJ/mol[84−86] for this RTIL. This energy is due to a contact ion pair transitioning from the liquid phase to the gas phase. Also, the cation−anion bond strength calculated for a single ion pair, is 305 kJ/mol.[87] Comparison of these three energies suggests that the micropore interaction is strong enough to modify the RTIL ion coordination structure, resulting in a high RTIL density due to the packing of ions that are less coordinated inside the micropores than in the bulk phase.

The micropore-confined RTIL number density, ρ_n, shows a higher density than the mesopore-confined RTIL. The ρ_n were integrated over the occupied volume to obtain ρ_{pore}/ρ_{bulk} for each simulation. The ρ_{pore}/ρ_{bulk} for the three RTIL-filled mesopores and micropore (in Figure 6b−e), are labeled ρ'_{MD} and plotted vs the corresponding f_{RTIL} in Figure 3. The micropore ρ'_{MD} is similar to the experimental result; about 3 times higher than the bulk density value. The mean density, $\rho'_{MD,ave}$, due to the combined effect of RTIL in the smooth cylindrical mesopores and in the micropores was calculated at each f_{meso}. The volumes v'_{mi} and v'_{meso} were used as weights to determine $\rho'_{MD,ave}$ for comparison with the ρ'_{SAXS} experimental results. This density is given by

$$\rho'_{MD,ave} = (v'_{mi}\rho'_{MD(mi)} + f_{meso}v'_{meso}\rho'_{MD(meso)}) / (v'_{mi} + f_{meso}v'_{meso})$$

Here, $\rho'_{MD(mi)}$ and $\rho'_{MD(meso)}$ are the ρ'_{MD} inside the micropores and mesopores at the corresponding filling fractions f_{meso}. For the micropore, $\rho'_{MD,ave} = \rho'_{MD(mi)}$. The $\rho'_{MD,ave}$ obtained by combining the simulations shown in Figure 6b−d with Figure 6e are shown in Figure 3 (*) and plotted vs f_{RTIL}. The simulations, which were carried out at similar f_{RTIL} as the experiment, show agreement in ρ_{pore}/ρ_{bulk} when the combined effect of both micropores and mesopores on the RTIL density are included.

These results are consistent with X-ray reflectivity results[88] from graphene in contact with bulk RTIL, which show local density fluctuations at the interface that are significantly higher than local fluctuations in the bulk liquid pair distribution function.[47] Comparison of surface structure results from X-ray reflectivity[88] and SFA[89] measurements with bulk structural properties[47] can help rationalize the current findings. X-ray reflectivity measurements have shown that the distance between the first density peak in the RTIL distribution perpendicular to a graphene surface is 3.2 Å, and SFA measurements have observed that a monolayer of cations is found within 3 Å from a mica surface.[89] For comparison, the first peak in the cation−anion radial distribution function for the bulk liquid is at 5.9 Å, with a local density fluctuation of almost twice the bulk value.[47] This demonstrates that the association with the surface is stronger than with neighboring ions and the average ion-wall distance is shorter than the ion−ion distance caused by electrostatic attraction. This shorter correlation distance, coupled with the reduced volume resulting from this specific micropore width, effectively truncates the ion density distribution that would otherwise exist at a single wall, thus resulting in a measured and simulated density which is significantly higher than the bulk value. The mean density values for samples S_1, S_2, S_3, and S_4, when averaged over the total pore volume, all display a higher density than the bulk. This effect is most noticeable at the lower RTIL f_{RTIL} values because they are more heavily weighed by the high RTIL density within the slitlike micropores.

CONCLUSION

The ability to extract quantitative information on the structure of room temperature ionic liquid (RTIL) electrolytes confined inside structurally complex carbon electrode porous materials has been demonstrated in the current work. The model developed, in which the measured properties may be described as a linear combination of mesopore and micropore effects, allow the molecular dynamics simulation to help describe the density of $[C_4mim^+]$ $[Tf_2N^-]$ inside a complex substrate. The density increase inside the micropores is due to the strong attraction of the ions to the surface, and to the relative size of the micropore compared to the ion dimensions. The typical cation−anion correlation distance in the bulk fluid is almost twice the ion−pore wall distance. Because the micropore dimension matches very closely the dimensions of the RTIL ions, there is minimal excluded volume in the filled micropore. Another effect of the close proximity of the slit pore walls is the high interaction potential with the RTIL, which is strong enough to modify the RTIL ion coordination structure, resulting in less coordinated ions inside the micropores than in the bulk fluid. The results presented herein are unique to interfacial phenomena and cannot be taken as a statement on the compressibility of a bulk RTIL fluid. Rather, the high densities correspond to the packing of ion pairs inside subnanometer pores. The two confining environments, namely the carbon mesopores and micropores, should also have a significant effect on the dynamic properties of this RTIL and further investigations in this area are warranted. This work provides experimental verification to recent work aimed at understanding ion/pore size/geometric effects in carbon supercapacitor systems,[30,90] and at describing the complex features of RTILs near surfaces, including the extent to which RTIL dissociation may occur.[91−93] This work highlights the importance of including the porous substrate's surface morphology, especially roughness and microporosity, in the characterization of the structural effects on the properties of RTILs for use in energy storage applications.

ASSOCIATED CONTENT

Supporting Information

Figure showing the effect of overfilling MC-127 with RTIL on the SAXS curve. This material is available free of charge via the Internet at http://pubs.acs.org.

AUTHOR INFORMATION

Corresponding Authors

*E-mail: banuelosjl@ornl.gov. Tel: 865-576-4870.
*E-mail: guang.feng@vanderbilt.edu. Tel: 615-322-8793.

Notes

The authors declare no competing financial interest.

■ ACKNOWLEDGMENTS

This work was supported as part of the Fluid Interface Reactions, Structures and Transport (FIRST) Center, an Energy Frontier Research Center funded by the U.S. Department of Energy, Office of Science, Office of Basic Energy Sciences. The SAXS portion of this research was conducted at the Center for Nanophase Materials Sciences, which is sponsored at Oak Ridge National Laboratory by the Scientific User Facilities Division, Office of Basic Energy Sciences, U.S. Department of Energy. The SANS portion of this research at Oak Ridge National Laboratory's Spallation Neutron Source was sponsored by the Scientific User Facilities Division, Office of Basic Energy Sciences, U.S. Department of Energy. G.F. thanks the Palmetto Cluster at Clemson University for providing computing resources. The authors would like to acknowledge C. Liao of the Chemical Sciences Division (CSD) at Oak Ridge National Laboratory (ORNL) for performing the anion exchange in the deuterated RTIL. The authors also acknowledge A.J. Rondinone and E.A. Payzant of ORNL for support with the SAXS setup, as well as C. Do and W. Heller of ORNL for beam line support during the SANS measurements.

■ REFERENCES

(1) Arico, A. S.; Bruce, P.; Scrosati, B.; Tarascon, J.-M.; Van Schalkwijk, W. *Nat. Mater.* **2005**, *4*, 366.
(2) Chmiola, J.; Yushin, G.; Gogotsi, Y.; Portet, C.; Simon, P.; Taberna, P. L. *Science* **2006**, *313*, 1760.
(3) Choi, B. G.; Yang, M.; Hong, W. H.; Choi, J. W.; Huh, Y. S. *ACS Nano* **2012**, *6*, 4020.
(4) Jeong, H.-K.; Jin, M.; Ra, E. J.; Sheem, K. Y.; Han, G. H.; Arepalli, S.; Lee, Y. H. *ACS Nano* **2010**, *4*, 1162.
(5) Kim, T. Y.; Lee, H. W.; Stoller, M.; Dreyer, D. R.; Bielawski, C. W.; Ruoff, R. S.; Suh, K. S. *ACS Nano* **2010**, *5*, 436.
(6) Inagaki, M.; Konno, H.; Tanaike, O. *J. Power Sources* **2010**, *195*, 7880.
(7) Liu, C.; Yu, Z.; Neff, D.; Zhamu, A.; Jang, B. Z. *Nano Lett.* **2010**, *10*, 4863.
(8) Conway, B. E. *Electrochemical Supercapacitors: Scientific Fundamentals and Technological Applications*; Kluwer Academic/Plenum: New York, 1999.
(9) Cheng, Q.; Tang, J.; Ma, J.; Zhang, H.; Shinya, N.; Qin, L.-C. *Phys. Chem. Chem. Phys.* **2011**, *13*, 17615.
(10) Korenblit, Y.; Rose, M.; Kockrick, E.; Borchardt, L.; Kvit, A.; Kaskel, S.; Yushin, G. *ACS Nano* **2010**, *4*, 1337.
(11) Pech, D.; Brunet, M.; Durou, H.; Huang, P. H.; Mochalin, V.; Gogotsi, Y.; Taberna, P. L.; Simon, P. *Nat. Nanotechnol.* **2010**, *5*, 651.
(12) Wu, Z.-S.; Ren, W.; Xu, L.; Li, F.; Cheng, H.-M. *ACS Nano* **2011**, *5*, 5463.
(13) Vu, A.; Li, X.; Phillips, J.; Han, A.; Smyrl, W. H.; Bühlmann, P.; Stein, A. *Chem. Mater.* **2013**.
(14) Kornyshev, A. A. *J. Phys. Chem. B* **2007**, *111*, 5545.
(15) Wu, J.; Jiang, T.; Jiang, D.-e.; Jin, Z.; Henderson, D. *Soft Matter* **2011**, *7*, 11222.
(16) Zhai, Y.; Dou, Y.; Zhao, D.; Fulvio, P. F.; Mayes, R. T.; Dai, S. *Adv. Mater.* **2011**, *23*, 4828.
(17) Wang, X.; Liang, C.; Dai, S. *Langmuir* **2008**, *24*, 7500.
(18) Fulvio, P. F.; Mayes, R. T.; Wang, X.; Mahurin, S. M.; Bauer, J. C.; Presser, V.; McDonough, J.; Gogotsi, Y.; Dai, S. *Adv. Funct. Mater.* **2011**, *21*, 2208.
(19) Castner, E. W.; Wishart, J. F. *J. Chem. Phys.* **2010**, *132*, 120901.
(20) Annapureddy, H. V. R.; Kashyap, H. K.; De Biase, P. M.; Margulis, C. J. *J. Phys. Chem. B* **2010**, *114*, 16838.
(21) Annapureddy, H. V. R.; Kashyap, H. K.; De Biase, P. M.; Margulis, C. J. *J. Phys. Chem. B* **2011**, *115*, 9507.
(22) Li, S.; Bañuelos, J. L.; Guo, J.; Anovitz, L. M.; Rother, G.; Shaw, R. W.; Hillesheim, P. C.; Dai, S.; Baker, G. A.; Cummings, P. T. *J. Phys. Chem. Lett.* **2011**, *3*, 125.
(23) Kislenko, S. A.; Samoylov, I. S.; Amirov, R. H. *Phys. Chem. Chem. Phys.* **2009**, *11*, 5584.
(24) Wang, S.; Li, S.; Cao, Z.; Yan, T. Y. *J. Phys. Chem. C* **2010**, *114*, 990.
(25) Vatamanu, J.; Borodin, O.; Smith, G. D. *J. Am. Chem. Soc.* **2010**, *132*, 14825.
(26) Shim, Y.; Kim, H. J. *ACS Nano* **2010**, *4*, 2345.
(27) Singh, R.; Monk, J.; Hung, F. R. *J. Phys. Chem. C* **2010**, *114*, 15478.
(28) Shim, Y.; Kim, H. J. *ACS Nano* **2009**, *3*, 1693.
(29) Wang, J.; Chu, H.; Li, Y. *ACS Nano* **2008**, *2*, 2540.
(30) Feng, G.; Cummings, P. T. *J. Phys. Chem. Lett.* **2011**, *2*, 2859.
(31) Wu, P.; Huang, J.; Meunier, V.; Sumpter, B. G.; Qiao, R. *ACS Nano* **2011**, *5*, 9044.
(32) Monk, J.; Singh, R.; Hung, F. R. *J. Phys. Chem. C* **2011**, *115*, 3034.
(33) Merlet, C.; Rotenberg, B.; Madden, P. A.; Taberna, P.-L.; Simon, P.; Gogotsi, Y.; Salanne, M. *Nat. Mater.* **2012**, *11*, 306.
(34) Feng, G.; Qiao, R.; Huang, J.; Dai, S.; Sumpter, B. G.; Meunier, V. *Phys. Chem. Chem. Phys.* **2011**, *13*, 1152.
(35) Israelachvili, J. N. *Intermolecular and Surface Forces*, 2nd ed.; Academic Press: New York, 1992.
(36) Niu, S. A.; Cao, Z.; Li, S.; Yan, T. Y. *J. Phys. Chem. B* **2010**, *114*, 877.
(37) Perkin, S. *Phys. Chem. Chem. Phys.* **2012**, *14*, 5052.
(38) Tokuda, H.; Hayamizu, K.; Ishii, K.; Susan, M.; Watanabe, M. *J. Phys. Chem. B* **2005**, *109*, 6103.
(39) Fredlake, C. P.; Crosthwaite, J. M.; Hert, D. G.; Aki, S. N. V. K.; Brennecke, J. F. *J. Chem. Eng. Data* **2004**, *49*, 954.
(40) Liu, H.; Maginn, E. *J. Chem. Phys.* **2011**, *135*, 124507.
(41) Russina, O.; Triolo, A.; Gontrani, L.; Caminiti, R.; Xiao, D.; Hines, L. G.; Bartsch, R. A.; Quitevis, E. L.; Pleckhova, N.; Seddon, K. R. *J. Phys.: Condens. Matter* **2009**, *21*, 1.
(42) Bodo, E.; Gontrani, L.; Caminiti, R.; Plechkova, N. V.; Seddon, K. R.; Triolo, A. *J. Phys. Chem. B* **2010**, *114*, 16398.
(43) Canongia Lopes, J. N.; Deschamps, J.; Pádua, A. A. H. *J. Phys. Chem. B* **2004**, *108*, 2038.
(44) Canongia Lopes, J. N.; Deschamps, J.; Pádua, A. A. H. *J. Phys. Chem. B* **2004**, *108*, 11250.
(45) Canongia Lopes, J. N.; Pádua, A. A. H. *J. Phys. Chem. B* **2004**, *108*, 16893.
(46) Köddermann, T.; Paschek, D.; Ludwig, R. *ChemPhysChem* **2007**, *8*, 2464.
(47) Zhao, W.; Eslami, H.; Cavalcanti, W. L.; Müller-Plathe, F. *Z. Phys. Chem.* **2007**, *221*, 1647.
(48) Sing, K. S. W.; Everett, D. H.; Haul, R. A. W.; Mouscou, L.; Pierotti, R. A.; Rouquerol, J.; Siemieniewska, T. *Pure Appl. Chem.* **1985**, *57*, 603.
(49) Maginn, E. J. *J. Phys.: Condens. Matter* **2009**, *21*, 1.
(50) Maginn, E. J. *Acc. Chem. Res.* **2007**, *40*, 1200.
(51) Lian, J.; Duan, X.; Ma, J.; Peng, P.; Kim, T.; Zheng, W. *ACS Nano* **2009**, *3*, 3749.
(52) Zheng, W.; Liu, X.; Yan, Z.; Zhu, L. *ACS Nano* **2008**, *3*, 115.
(53) Swatloski, R. P.; Spear, S. K.; Holbrey, J. D.; Rogers, R. D. *J. Am. Chem. Soc.* **2002**, *124*, 4974.
(54) Samayam, I. P.; Hanson, B. L.; Langan, P.; Schall, C. A. *Biomacromolecules* **2011**, *12*, 3091.
(55) Kang, Y. J.; Chun, S.-J.; Lee, S.-S.; Kim, B.-Y.; Kim, J. H.; Chung, H.; Lee, S.-Y.; Kim, W. *ACS Nano* **2012**, *6*, 6400.
(56) Wang, X. Q.; Liang, C. D.; Dai, S. *Langmuir* **2008**, *24*, 7500.
(57) Burrell, A. K.; Sesto, R. E. D.; Baker, S. N.; McCleskey, T. M.; Baker, G. A. *Green Chem.* **2007**, *9*, 449.
(58) Kline, S. *J. Appl. Crystallogr.* **2006**, *39*, 895.
(59) Lindahl, E.; Hess, B.; van der Spoel, D. *J. Mol. Modell.* **2001**, *7*, 306.
(60) Borodin, O. *J. Phys. Chem. B* **2009**, *113*, 11463.

(61) Bedrov, D.; Borodin, O.; Li, Z.; Smith, G. D. *J. Phys. Chem. B* **2010**, *114*, 4984.
(62) Yeh, I. C.; Berkowitz, M. L. *J. Chem. Phys.* **1999**, *111*, 3155.
(63) Hess, B.; Bekker, H.; Berendsen, H. J. C.; Fraaije, J. G. E. M. *J. Comput. Chem.* **1997**, *18*, 1463.
(64) Kruk, M.; Jaroniec, M.; Gadkaree, K. P. *J. Colloid Interface Sci.* **1997**, *192*, 250.
(65) Jaroniec, M.; Solovyov, L. A. *Langmuir* **2006**, *22*, 6757.
(66) Choma, J.; Górka, J.; Jaroniec, M. *Microporous Mesoporous Mater.* **2008**, *112*, 573.
(67) Kruk, M.; Jaroniec, M. *Chem. Mater.* **2001**, *13*, 3169.
(68) Hu, N.; Borkar, N.; Kohls, D.; Schaefer, D. W. *J. Membr. Sci.* **2011**, *379*, 138.
(69) Schaefer, D. W.; Pekala, R.; Beaucage, G. *J. Non-Cryst. Solids* **1995**, *186*, 159.
(70) Schaefer, D. W.; Keefer, K. D. *Phys. Rev. Lett.* **1986**, *56*, 2199.
(71) Guinier, A.; Fournet, G. *Small-Angle Scattering of X-rays*; John Wiley & Sons: New York, 1955.
(72) Glatter, O.; Kratky, O. *Small-Angle X-ray Scattering*; Academic Press: New York, 1982.
(73) Porod, G. *Kolloid Z* **1951**, *124*, 32.
(74) Ciccariello, S.; Riello, P. *J. Appl. Crystallogr.* **2007**, *40*, 282.
(75) Beaucage, G. *J. Appl. Crystallogr.* **1996**, *29*, 134.
(76) Teixeira, J. *J. Appl. Crystallogr.* **1988**, *21*, 781.
(77) Bale, H. D.; Schmidt, P. W. *Phys. Rev. Lett.* **1984**, *53*, 596.
(78) Lin, M. Y.; Sinha, S. K.; Drake, J. M.; Wu, X. l.; Thiyagarajan, P.; Stanley, H. B. *Phys. Rev. Lett.* **1994**, *72*, 2207.
(79) Wu, W.-l. *Polymer* **1982**, *23*, 1907.
(80) Anderson, J. L.; Dixon, J. K.; Brennecke, J. F. *Acc. Chem. Res.* **2007**, *40*, 1208.
(81) Stefanopoulos, K. L.; Romanos, G. E.; Vangeli, O. C.; Mergia, K.; Kanellopoulos, N. K.; Koutsioubas, A.; Lairez, D. *Langmuir* **2011**, *27*, 7980.
(82) Jaroniec, C. P.; Kruk, M.; Jaroniec, M.; Sayari, A. *J. Phys. Chem. B* **1998**, *102*, 5503.
(83) Kruk, M.; Jaroniec, M.; Sayari, A. *Langmuir* **1999**, *15*, 5683.
(84) Santos, L. M. N. B. F.; Canongia Lopes, J. N.; Coutinho, J. A. P.; Esperança, J. M. S. S.; Gomes, L. R.; Marrucho, I. M.; Rebelo, L. P. N. *J. Am. Chem. Soc.* **2006**, *129*, 284.
(85) Zaitsau, D. H.; Kabo, G. J.; Strechan, A. A.; Paulechka, Y. U.; Tschersich, A.; Verevkin, S. P.; Heintz, A. *J. Phys. Chem. A* **2006**, *110*, 7303.
(86) Kelkar, M. S.; Maginn, E. J. *J. Phys. Chem. B* **2007**, *111*, 9424.
(87) Fernandes, A. M.; Rocha, M. A. A.; Freire, M. G.; Marrucho, I. M.; Coutinho, J. o. A. P.; Santos, L. s. M. N. B. F. *J. Phys. Chem. B* **2011**, *115*, 4033.
(88) Zhou, H.; Rouha, M.; Feng, G.; Lee, S. S.; Docherty, H.; Fenter, P.; Cummings, P. T.; Fulvio, P. F.; Dai, S.; McDonough, J.; Presser, V.; Gogotsi, Y. *ACS Nano* **2012**, *6*, 9818.
(89) Perkin, S.; Crowhurst, L.; Niedermeyer, H.; Welton, T.; Smith, A. M.; Gosvami, N. N. *Chem. Commun.* **2011**, *47*, 6572.
(90) Feng, G.; Li, S.; Presser, V.; Cummings, P. T. *J. Phys. Chem. Lett.* **2013**, 3367.
(91) Gebbie, M. A.; Valtiner, M.; Banquy, X.; Fox, E. T.; Henderson, W. A.; Israelachvili, J. N. *Proc. Natl. Acad. Sci.* **2013**, *110*, 9674.
(92) Perkin, S.; Salanne, M.; Madden, P.; Lynden-Bell, R. *Proc. Natl. Acad. Sci.* **2013**, *110*, E4121.
(93) Gebbie, M. A.; Valtiner, M.; Banquy, X.; Henderson, W. A.; Israelachvili, J. N. *Proc. Natl. Acad. Sci.* **2013**, *110*, E4122.